Tectonophysics 918 (2026) 230970

Contents lists available at ScienceDirect

Tectonophysics

journal homepage: www.elsevier.com/locate/tecto

Deep permeability architecture of a detachment fault: Constraints from in situ borehole samples in Triassic evaporite-carbonate sequences beneath the frontal Longmen Shan, China

Lin Zhang [a,b], Yi Li [a], Qingbao Duan [b], Shunjie Deng [a], Nianfa Yang [c], Huayao Zou [a], Jianye Chen [b], Zonghu Liao [a,*]

[a] China-Portugal Joint Research Institute of Climate and Energy, China University of Petroleum (Beijing), Beijing, China
[b] State Key Laboratory of Earthquake Dynamics and Forecasting, Institute of Geology, China Earthquake Administration, Beijing, China
[c] PetroChina Zhejiang Oilfield Company, Hangzhou, China

ARTICLE INFO

Keywords:
Evaporite-carbonate
Permeability structure
Deep borehole samples
Pore pressure oscillation
Seismogenic

ABSTRACT

Fault damage zone permeability governs fluid migration, fault mechanics, and seismic rupture dynamics. Here, we investigate the permeability structure of the Triassic damaged stratigraphy beneath the frontal Longmen Shan fault system—a key structure within the Sichuan Basin—through direct analysis of deeply drilled core samples (~6800 m depth) from the LS1 borehole. We integrated mineralogical analyses, permeability measurements under in situ stress conditions (5–125 MPa effective pressure) using the pore pressure oscillation (PPO) method with distilled water, and microstructural observations. X-ray diffraction (XRD) results reveal a pronounced mineralogical contrast between intact and damaged fault-zone samples. The intact anhydrite (Anh-01) is dominated by anhydrite (~89 %) with minor dolomite (~10 %), whereas the mixed dolostone-anhydrite cataclasites (Dol-Anh-01 and Dol-Anh-02) contain progressively higher dolomite (40–93 %) and illite (1–6 %), together with accessory quartz, feldspars, and trace gypsum. The co-occurrence of soluble feldspars and illite indicates fluid-mediated alteration and phyllosilicate network development during cataclastic deformation, consistent with fluid-rock interaction documented in active fault zones. Permeability decreases nonlinearly with increasing effective pressure: a sharp reduction at 5–25 MPa likely reflects fracture closure, followed by gradual compaction at 40–125 MPa. The damage lithology, rich in brittle dolomite-anhydrite fragments (>40 %), shows permeability of 10^{-20}–10^{-18} m^2, whereas the intact anhydrite exhibits lower values (10^{-21}–10^{-19} m^2). Permeability anisotropy arises from (i) brittle block abundance, (ii) weak-phase alignment (e.g., clay films along microfractures), and (iii) mineralogically driven pore-network heterogeneity. We propose a dynamic permeability model in which seismic slip enhances fracture connectivity (permeability surge), followed by postseismic self-sealing through compaction and mineralization—a feedback mechanism modulating fluid overpressures and recurrence intervals. This study provides the first in situ constraints on the hydromechanical behavior of an evaporite-carbonate damaged stratigraphy at seismogenic depths in Longmen Shan range. The results challenge assumptions of static permeability in fault models and highlight the necessity of integrating lithological heterogeneity and transient hydraulic processes in seismic hazard assessments.

1. Introduction

Permeability is a fundamental hydraulic property that controls fluid transport and fluid-rock interactions, with direct consequences for fault strength and slip behavior (Chester et al., 1993; Evans and Chester, 1995; Bos and Spiers, 2002; Molli et al., 2010; Leclere et al., 2016). Although the permeability of crystalline and sedimentary rocks has been extensively studied for decades (Schon, 1996; Bense et al., 2013; Scibek, 2020), recent research has increasingly focused on fault-related rocks from natural fault zones (e.g., Wibberley and Shimamoto, 2003; Tsutsumi et al., 2004; Uehara and Shimamoto, 2004; Agosta et al., 2007; Haines et al., 2016).

Fluids, such as groundwater and hydrocarbons, play a crucial role in fault mechanics and seismic activity (Zoback and Harjes, 1997;

* Corresponding author.
E-mail address: zong@cup.edu.cn (Z. Liao).

https://doi.org/10.1016/j.tecto.2025.230970
Received 18 May 2025; Received in revised form 24 October 2025; Accepted 25 October 2025
Available online 26 October 2025

Sutherland et al., 2012; Ross et al., 2020; Dvory and Zoback, 2021; Curzi et al., 2024; Smeraglia et al., 2022). Field and laboratory studies demonstrate that mature faults can act as barriers, conduits, or hybrid systems, significantly influencing fluid flow in the upper crust (Antonellini and Aydin, 1994; Caine et al., 1996; Lacroix et al., 2012; Smeraglia et al., 2020). The internal architecture of mature faults—typically composed of a highly strained fault core, a fractured damage zone, and a relatively intact protolith—varies depending on deformation history, host-rock lithology, and faulting conditions (Chester et al., 1993; Sagy et al., 2001; Kim et al., 2004; Savage and Brodsky, 2011). These variations complicate predictions of fluid transport behavior (Faulkner et al., 2010).

Permeability measurements are commonly obtained using three main approaches: (1) in situ borehole-based techniques such as water-injection or tidal-response experiments; (2) laboratory measurements on surface outcrop samples; and (3) laboratory measurements on borehole core samples (e.g., Ohtake, 1974; Kitagawa et al., 1999; Wibberley and Shimamoto, 2003; Mizoguchi et al., 2008; Xue et al., 2013; Smeraglia et al., 2014; Yan et al., 2016; Scibek, 2020). While in situ techniques provide permeability data under natural conditions, they yield bulk averages over large volumes—often spanning hundreds of meters around the borehole (Wilson et al., 1979; Kitagawa et al., 1999; Guo et al., 2021)—and therefore cannot resolve fine-scale heterogeneities within complex fault zones. In contrast, laboratory measurements offer higher spatial resolution and better control of experimental parameters. However, surface outcrop samples typically display permeability values nearly one order of magnitude higher than those of corresponding borehole samples (Trippetta et al., 2010), likely due to stress release during exhumation.

Recent advances in fault zone permeability research have largely come from laboratory studies of samples collected from major fault systems, including the Nojima Fault (Lockner et al., 2000; Mizoguchi et al., 2008), the Median Tectonic Line in Japan (Wibberley and Shimamoto, 2003), the Parasano Fault (Agosta et al., 2007); the Chelungpu Fault (Tanikawa and Shimamoto, 2009), the Japan Trench plate boundary (Tanikawa et al., 2013), the San Andreas Fault (Morrow et al., 2014), the Yinxiu-Beichuan Fault (Chen et al., 2013; Duan et al., 2017), and the Gole Larghe Fault (Rempe et al., 2018). However, most of these studies rely on surface outcrops or shallow boreholes samples, raising questions about their applicability to deeper fault zones (e.g., 6000–7000 m) (Townend and Zoback, 2000; Mizoguchi et al., 2008; Uehara et al., 2012; Morrow et al., 2014).

In this study, we investigate the hydraulic structure of the Triassic detachment fault beneath the frontal Longmen Shan by analyzing deep-borehole (LS1, ~6900 m) core samples. Laboratory experiments were conducted on evaporite-carbonate fault rocks obtained from within the detachment zone (Figs. 1). By integrating mineralogical characterization, high-pressure permeability measurements, and microstructural observations, we quantify the fluid transport properties and propose a model for permeability evolution throughout the seismic cycle.

2. Geological setting

The Longmen Shan (LMS) marks a pronounced topographic and tectonic transition between the high-elevation Tibetan Plateau and the low-lying Sichuan Basin (SCB) in China (Fig. 1A). The LMS thrust belt comprises a series of NE-striking thrust faults, including (from west to east) the Qingchuan-Maowen fault, Beichuan-Yingxiu fault, Pengguan fault, Guankou fault, and Pengxian fault (Burchfiel et al., 1995; Jia et al., 2006; Hubbard et al., 2010; Lu et al., 2019). This active thrust belt extends for approximately 500 km in length and 30–50 km in width, and is traditionally subdivided into northern, central, and southern segments, with internal boundaries near Dujiangyan and Anxian (Molnar and Tapponnier, 1975; Burchfiel et al., 1995; Liu et al., 2009; Li et al., 2012).

The LMS has experienced two major orogenic phases since the early Mesozoic (~250 Ma): (1) Late Triassic compressional and (2) Cenozoic deformation associated with the India-Asian collision (Burchfiel et al., 1995; Chen and Wilson, 1996; Jia et al., 2006). The central LMS exposes predominantly Mesozoic strata (Chen et al., 1995; Liu et al., 1996), where shallow structural features are characterized by imbricated thrusts and ramp-fold structures (Hubbard and Shaw, 2009; Jia et al., 2010; Lu et al., 2012).

Surface mapping and drilling data reveal that the central LMS cover sequence consists of Sinian to Middle Triassic shallow-marine clastic and evaporite-carbonate rocks, overlain by Late Triassic terrestrial deposits. Eastward, the Sichuan Basin contains more than 5 km of clastic rocks (Li et al., 1995; Chen et al., 1995), resting on a Precambrian crystalline basement. Integration of drilling, seismic reflection, and surface geological data indicates two principal detachment fault zones in the frontal central LMS: (1) a deep Precambrian detachment (~15–17 km depth) characterized by strong frictional behavior; and (2) a shallower Triassic detachment (~6.5 km depth) dominated by ductile deformation (Jia et al., 2010; Li et al., 2018; Zhang et al., 2022; Liao et al., 2023). The Middle-Lower Triassic detachment is particularly significant because it governs upper-crustal deformation and seismicity distribution along the LMS range front (Li et al., 2016; Lu et al., 2019; Liao et al., 2023). Recent seismic activity associated with this detachment includes the 2013 M_w 6.6 Lushan earthquake, which was generated by a ramp within the Range Front blind thrust (RFBT) that merges upward with the detachment level in the Sichuan Basin at ~4–6 km depth (Wang et al., 2014). In this study, we focus on the permeability characterization of fault rocks from this Triassic detachment zone within evaporite-carbonate units (Fig. 1).

3. Methods

The experiments were conducted on three representative lithologies, including an intact anhydrite (Anh-01) and two mixed dolostone-anhydrite cataclasites that differ in damage intensity—highly fractured (Dol-Anh-01) and weakly fractured (Dol-Anh-02). These lithologies were collected from depths of 6874.1 m, 6875.9 m, and 6877.3 m, respectively. For XRD analyses, one representative specimen from each lithology was selected. For permeability measurements, two specimens from each category—cored parallel (||) and perpendicular (⊥) to the drilling axis—were tested to evaluate the influence of anisotropy on permeability. In addition, ten thin sections of anhydrite and mixed dolostone-anhydrite cataclasite were analyzed to characterize their microstructural features.

3.1. X-ray diffraction analysis

X-ray diffraction (XRD) analysis was systematically performed to quantify both bulk-rock composition and clay mineral content using the normalized reference intensity ratio (RIR) method (Hubbard et al., 1976). This approach leverages the proportional relationship between mineral peak intensities and their modal abundances in polyphase mixtures.

3.2. Permeability and porosity measurements

Permeability measurements were conducted at the Institute of Geology, China Earthquake Administration (CEA), using a high-pressure fluid-flow system capable of operating with either gaseous or aqueous permeants. The experimental setup employed the pore-pressure-oscillation (PPO) method (Fischer, 1992; Fischer and Paterson, 1992), which determines hydraulic properties through differential-pressure analysis between upstream and downstream reservoirs. Pore pressures were measured using DRUCK PTX 610 pressure transducers with a precision of ±0.032 MPa. The detection limits of the system are approximately 10^{-22} m^2 for permeability and 10^{-12} Pa^{-1} for specific storage (Chen et al., 2015; Duan et al., 2017). In brief, a sinusoidal pressure signal was applied at the upstream end of the sample, and the

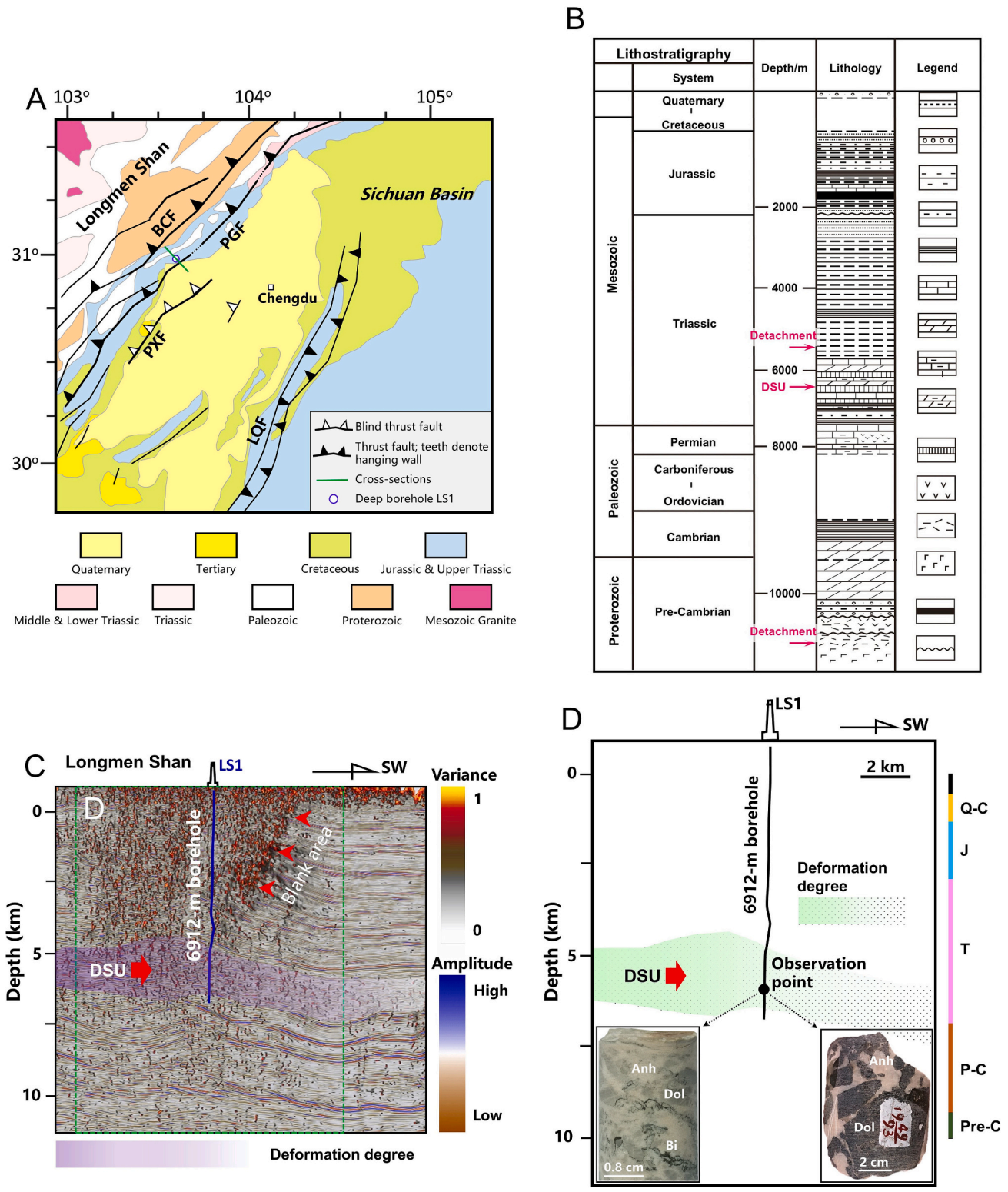

Fig. 1. (A) Regional geologic map of the Longmen Shan and the western Sichuan Basin, showing major faults (black lines), exposed stratigraphy (after Li et al., 2012), and the location of borehole LS1. BCF: Beichuan fault; PGF: Pengguan fault; PXF: Pengxian fault; LQF: Longquan fault. (B) Sedimentary stratigraphy of the Pengzhou area (modified from Lu et al., 2019). (C) Interpreted, depth-converted 3D seismic reflection profile co-rendered with seismic variance data from the piedmont region of the central Longmen Shan (location marked by the green line in Fig. 1A). Small red triangles indicate the position of the frontal thrust system of the Longmen Shan. The term 'Damaged Stratigraphic Unit (DSU)' refers to a dynamically evolved detachment zone within the Triassic brittle-ductile complex sedimentary sequences (cf. Liao et al., 2023). (D) Vertical projection of borehole LS1 (location marked by the green rectangle in Fig. 1B). Anh: Anhydrite; Dol: Dolomite; Bi: Bitumen. Q-C: Quaternary-Cretaceous; J: Jurassic; T: Triassic; P-C: Permian-Cambrian; Pre-C: Pre-Cambrian. (For interpretation of the references to colour in this figure legend, the reader is referred to the web version of this article.)

downstream response was recorded. Fourier analysis of these signals yielded the amplitude ratio and phase delay. Using these two parameters, dimensionless coefficients were calculated according to Fischer (1992) and Fischer and Paterson (1992), from which the sample's permeability and specific storage were derived.

Sample porosity was determined by first measuring the absolute porosity at the initial pressure and then assessing porosity changes in response to incremental pressure steps. Absolute porosity was measured using a microvolumeter equipped with a needle valve and a high-precision displacement sensor (resolution = 0.001 mm). Changes in porosity were inferred from induced pore pressure variation, using distilled water as the pore fluid and assuming that the total volumetric change equaled the change in pore volume within the specimen.

3.3. Sample preparation and testing conditions

Sample preparation followed strict protocols:

- Cylindrical specimens (Ø20 mm, L5–15 mm) were cored with parallel and perpendicular orientations to drilling axis (Fig. 2; Table 1)
- Samples were categorized by burial depth and lithology into three groups
- All specimens were oven-dried at 65 °C to relative constant mass (~12 h)

Test conditions maintained:

- Confining pressures (Pc) up to 140 MPa
- Constant pore pressure (Pp = 15 MPa) using distilled water
- Room temperature environment

Detailed experimental procedure followed established procedures (cf. Chen et al., 2015; Duan et al., 2017): (1) Load the confining pressure to 8 MPa and evacuate the pore-fluid pipelines. Measure the initial porosity using nitrogen gas. (2) Evacuate the pipelines again and introduce distilled water to saturate the flow lines and the sample. Synchronously increase the confining pressure to 20 MPa and pore pressure to 15 MPa. (3) Measure the permeability and specific storage using the PPO method. (4) Change the confining pressure and record the induced pore pressure variation to calculate the porosity change. (5) Repeat steps (3) and (4) at each confining-pressure increment. Following this procedure, with confining pressure varied (both loading and unloading) between 20 MPa and 140 MPa, a complete dataset of hydraulic properties—including permeability, porosity, and specific storage—was obtained. The experimental design specifically addresses the need for high-pressure conditions representative of in situ stress states at the sampled depths.

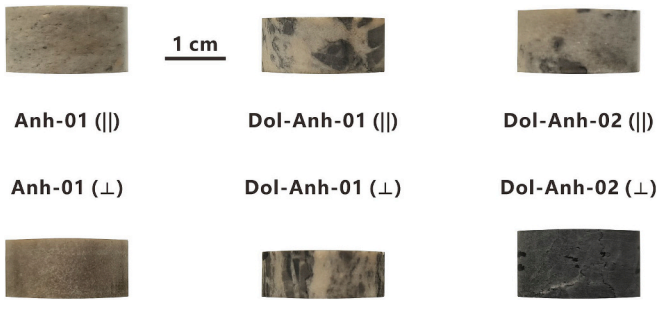

Fig. 2. Representative hand specimens of evaporite-carbonate fault rocks collected from a depth of ~6800 m. The samples include intact anhydrite (Anh-01) and mixed dolostone-anhydrite cataclasite (Dol-Anh-01 and Dol-Anh-02), each prepared with core orientations both parallel (||) and perpendicular (⊥) to the drilling direction. The samples display a heterogeneous distribution of dolostone clasts embedded within a fine-grained anhydrite matrix. The orientation definitions "||" and "⊥" also apply to Figs. 3–4 and Tables 1–2.

Table 1
Specification of the core samples and initial experimental results.

Rock type	Sample ID	Length (cm)	Diameter (cm)	Φ_0 (%)	k_0 (10^{-19} m^2)
Anhydrite	Anh-01 (||)	1.188	2.04	1.18	4.054
	Anh-01 (⊥)	1.063	2.032	–	0.479
Dolomite & Anhydrite	Dol-Anh-01 (||)	0.875	2.033	1.31	32.142
	Dol-Anh-01 (⊥)	0.750	2.027	0.43	26.154
	Dol-Anh-02 (||)	1.125	2.029	0.45	3.757
	Dol-Anh-02 (⊥)	1.125	2.029	0.68	29.531

"–" denotes content below detection; the same notation also applies to Table 2.

3.4. Permeability-pressure relationship

Previous studies have shown that both exponential and power-law relationships can adequately model permeability-pressure behavior (Morrow et al., 1986; Faulkner, 2004; Duan et al., 2017). In this study, we adopted the exponential law (David et al., 1994), expressed as:

$$k = k_0 \exp[-\gamma(P_e - P_0)] \quad (1)$$

where k is the permeability at effective pressure P_e, k_0 is the initial permeability at reference pressure P_0 (taken as atmospheric pressure, 0.1 MPa), and γ is the pressure sensitivity coefficient, which is lithology-dependent and influenced by fracture density, pore structure, and mineral filling (cf. Berryman, 1992; Evans et al., 1997; Ghabezloo and Sulem, 2009).

4. Experimental results

4.1. Mineralogical characterization via XRD analysis

XRD analysis reveals significant mineralogical contrasts between intact and damaged fault zone samples (Figs. 3, S1-S6). The intact sample (Anh-01) is overwhelmingly dominated by anhydrite (89 %) with subordinate dolomite (10.5 %) and only trace gypsum (0.5 %), indicating minimal post-depositional alteration. In marked contrast, damaged samples exhibit substantially more complex mineral assemblages. Dol-Anh-01 contains nearly equal proportions of anhydrite (53.6 %) and dolomite (40 %), along with accessory quartz (2.4 %), K-feldspar (2.4 %), plagioclase (0.4 %), and illite (1 %). Dol-Anh-02, in contrast, is overwhelmingly dolomitic (92.9 %) with minor anhydrite (0.7 %), quartz (0.5 %), and significantly higher illite content (5.9 %).

4.2. Permeability results

Integrated measurements of permeability, porosity and specific storage were conducted on six samples obtained from the LS1 deep borehole. The experimental results are plotted as functions of Terzaghi effective pressure ($P_e = P_c - P_p$, where P_e is effective pressure, P_c is confining pressure, and P_p is pore pressure) for both loading (pressurizing) and unloading (de-pressurizing) paths (Fig. 4). Sample information and initial measurements are summarized in Table 1. Owing to the extremely low initial porosities (generally < 1%; see Table 1), cross-plots of porosity versus effective pressure were not obtained.

Permeability decreases rapidly as Pe increases to ~30 MPa, followed by a more gradual decline from 40 MPa to 125 MPa (Fig. 4). During unloading, permeability increases slightly as Pe decreases from 125 MPa to 5 MPa. Across the entire effective pressure range investigated, sample permeabilities span nearly three orders of magnitude. The intact

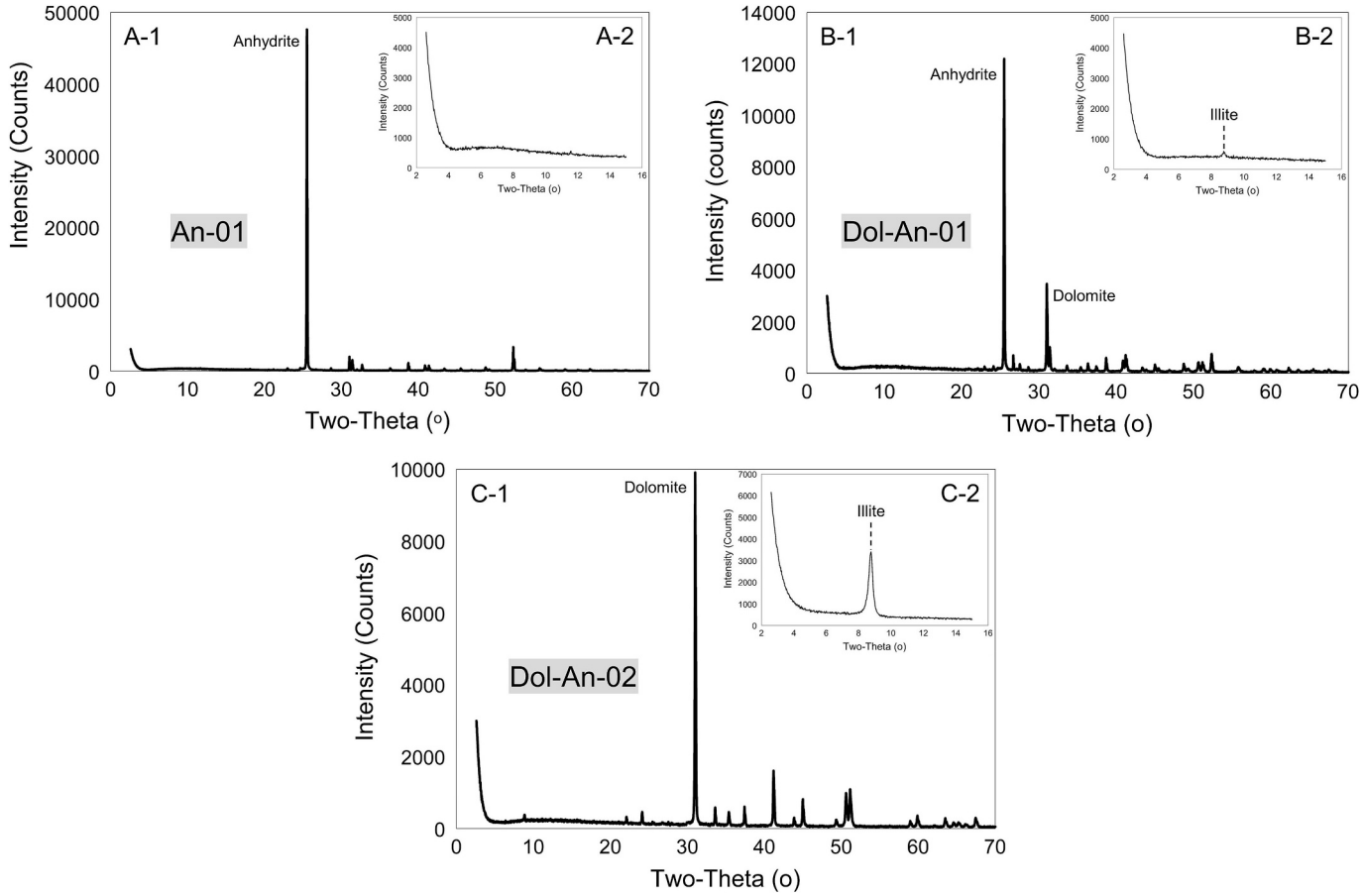

Fig. 3. X-ray diffraction (XRD) patterns of anhydrite, dolomite, and clay minerals from deformed samples collected within the evaporite-carbonate-hosted Middle-Lower Triassic detachment fault zone. (A-1) Powder XRD spectrum of sample Anh-01 (||) from the intact unit, predominantly composed of anhydrite. (A-2) XRD pattern of clay minerals extracted from the same sample (corresponding to A-1). (B-1) Powder XRD spectrum of sample Dol-Anh-01 (||) from the damage unit, composed mainly of anhydrite and dolostone. (B-2) XRD pattern of clay minerals corresponding to B-1. (C-1) Powder XRD spectrum of sample Dol-Anh-02 (⊥) from the damage unit, also dominated by anhydrite and dolostone. (C-2) XRD pattern of clay minerals corresponding to C-1.

anhydrite (Anh-01) exhibits the lowest permeability, ranging from 7.79×10^{-21} m^2 to 7.05×10^{-19} m^2. Permeability evolution and magnitude are also influenced by sample orientation (Fig. 4A-B). Specifically, under the same effective-stress interval, the permeability change in the sample cored parallel to the drilling direction is nearly twice that of sample cored perpendicular to it. In contrast, the damaged samples (Dol-Anh-01 and Dol-Anh-02), composed primarily of dolomite and anhydrite, display permeability values approximately one order of magnitude higher, ranging from 1.22×10^{-20} m^2 to 3.64×10^{-18} m^2 (Fig. 4C-F). Comparison between these two damaged samples indicates that permeability is inversely correlated with the degree of accommodated strain, progressively decreasing toward the intact protolith. To quantify permeability evolution with pressure (depth), experimental data were fitted using the exponential relation (Eq. (1)). Fitting results are presented in Fig. 4 and summarized in Table 1. The initial average permeability (k_0) for the intact anhydrite (Anh-01) and damaged samples (Dol-Anh-01 and Dol-Anh-02) are 2.27×10^{-19} m^2, 2.92×10^{-18} m^2, and 1.67×10^{-18} m^2, respectively, indicating that the intact unit is approximately one order of magnitude less permeable. The corresponding pressure sensitivity coefficients (γ) range from 0.016 MPa^{-1} to 0.018 MPa^{-1} for Anh-01, 0.032 MPa^{-1} to 0.049 MPa^{-1} for Dol-Anh-01, and 0.024 MPa^{-1} to 0.048 MPa^{-1} for Dol-Anh-02.

4.3. Microstructural characteristics of anhydrite-dolostone cataclasite

Our samples, obtained from a depth of approximately 6800 m, consist predominantly of anhydrite and dolostone (Figs. 2, 5), representing conditions that strongly favor complete dehydration (Table 2; e.g., De Paola et al., 2008). Fig. 5 illustrates several key microstructural features: (1) Fine-grained crystals (<500 μm) exhibit pervasive planar alignment (Fig. 5A-B), with elongated grains showing preferred orientations parallel/oblique to shear direction (Fig. 3B). (2) Dolostone fragments are embedded within ductile anhydrite layers and show evidence of progressive fragmentation under increasing shear strain (Fig. 5C-E). (3) Dolostone fractures are entirely sealed by anhydrite crystals and bitumen, leaving no observable pore space (Fig. 5C, E). (4) Distinct feldspar alteration halos along dolostone clast margins (Fig. 5D-E) indicate post-deformation fluid infiltration.

5. Discussion

5.1. Permeability characteristics and seismic cycle implications

Permeability measurements on six samples from the Middle-Lower Triassic detachment fault zone reveal a broadly consistent two-stage evolution with effective pressure and systematic variations across structural domains. Permeability decreases with increasing effective pressure in two distinct stages: an initial rapid drop up to ~30 MPa, followed by a more gradual decline at higher pressures (Fig. 4). The initial sharp reduction is attributed to fracture closure, whereas the subsequent decrease reflect pore-space compaction (cf. David et al., 2001; Mizoguchi et al., 2008; Wang et al., 2017). Damage zone samples, characterized by dolomite-rich compositions (>40 % dolomite with

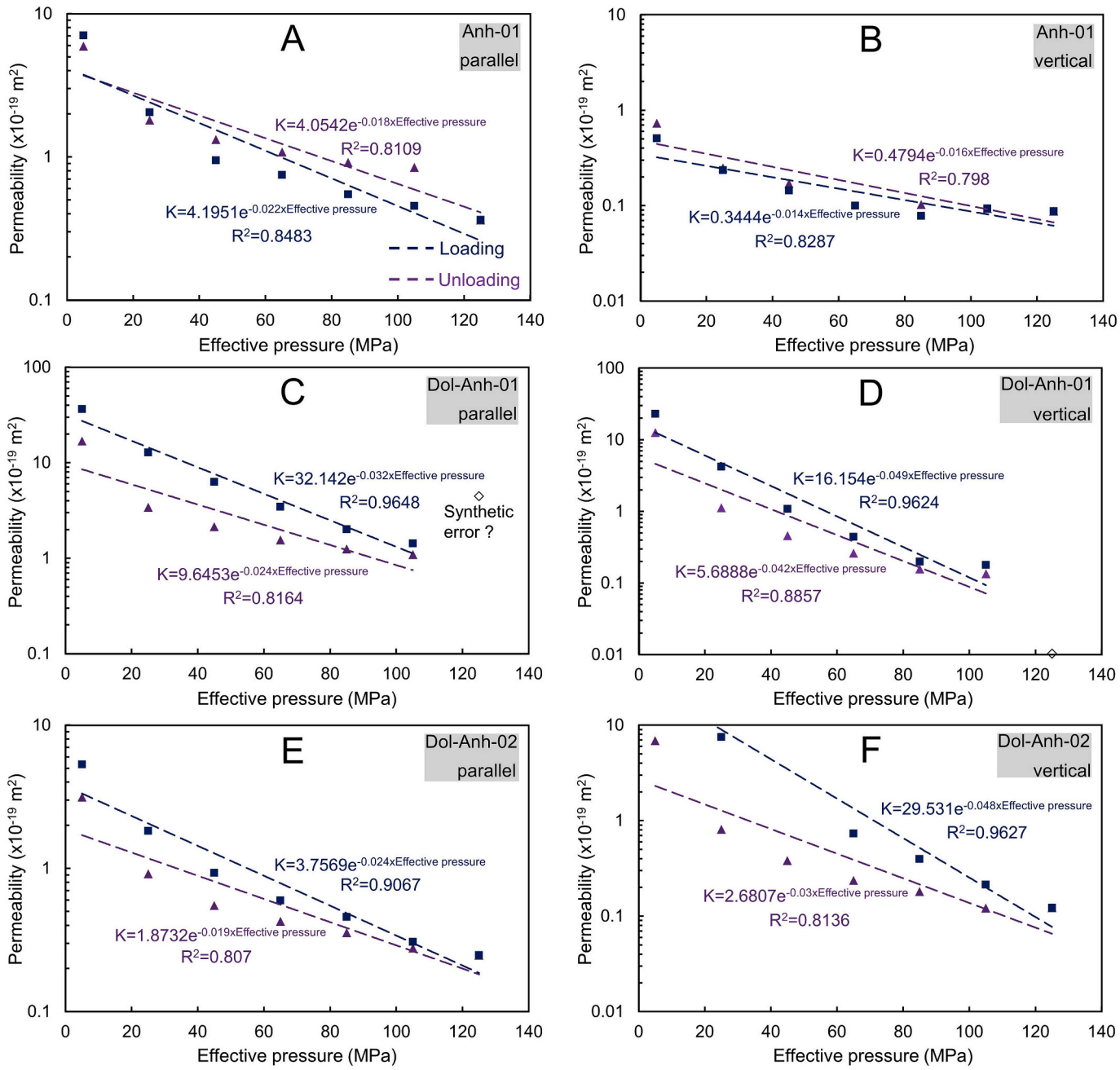

Fig. 4. Hydrostatic permeability of fault-related rocks plotted as a function of effective pressure. (A) Results for sample Anh-01 (||) from the intact unit. (B) Results for sample Anh-01 (⊥) from the intact unit. (C) Results for sample Dol-Anh-01 (||) from the damage unit. (D) Results for sample Dol-Anh-01 (⊥) from the damage unit. (E) Results for sample Dol-Anh-02 (||) from the damage unit. (F) Results for sample Dol-Anh-02 (⊥) from the damage unit. Because there are only two data points below 30 MPa, we chose to apply a global fit. Except for Anh-01(||)—where new fractur space may have formed during pressurization—the loading permeability curves for all other samples plot above their unloading curves.

anhydrite), exhibit relatively higher permeability (1.22×10^{-20} to 3.64×10^{-18} m^2) compared to intact anhydrite-dominated samples (~89 % anhydrite; 7.79×10^{-21} to 7.05×10^{-19} m^2), although the contrast remains within about one order of magnitude. Notably, permeability systematically decreases from highly deformed to less deformed zones in aligned fault rocks, independent of fracture filling state. The permeability range of our intact anhydrite sample algins with the results of Trippetta et al. (2010) for intact sulphate and dolostone samples, where increasing effective pressure from 10 MPa to 90 MPa reduced permeability from 10^{-18} m^2 to 10^{-22} m^2 with minor perturbations. Those authors also showed that borehole samples exhibited permeability values nearly one order of magnitude lower than equivalent outcrop samples under the same loading conditions. Our intact sample (dominated by anhydrite) shows a permeability range of 10^{-21} m^2 to 10^{-19} m^2, approximately one order of magnitude higher than the outcrop samples reported by Trippetta et al. (2010) (10^{-22} to 10^{-20} m^2), likely due to the presence of brittle breccias within the anhydrite matrix (Table 2). De Paola et al. (2008) indicated that dolomite blocks act as rigid inclusions below the brittle-ductile transition of anhydrite, rotating and fracturing within the ductile anhydrite matrix. In this context, dolostone fragments can exert strong control on the bulk permeability of the fault rock (Trippetta et al., 2010). Moreover, well-developed mineralogical transformations—particularly the formation of phyllosilicate networks through ongoing fluid-rock interaction—can modulate

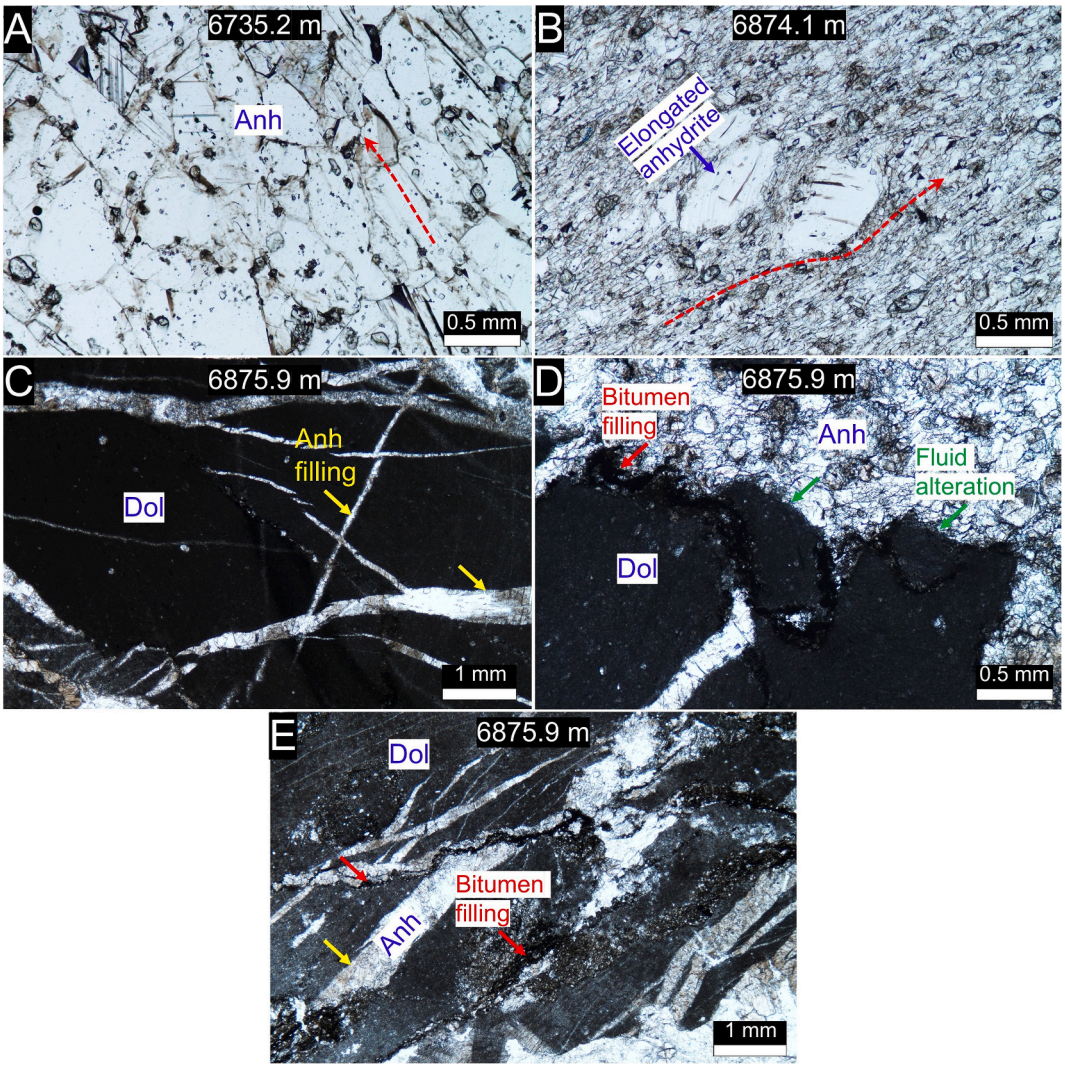

Fig. 5. Photomicrographs of thin sections from core samples obtained from borehole LS1 (see Fig. 1A), illustrating microstructural features of both intact units (A-B) and damage zone (C-E). The images highlight flow structures of anhydrite (light gray to white), along with fractures and cataclastic textures in dolostone (dark gray). Sample depths are indicated at the top center of each image. Notable features include anhydrite filling (yellow arrow), bitumen filling (red arrow), and fluid alteration (green arrow). All photomicrographs (A-E) were taken under plane-polarized light. (For interpretation of the references to colour in this figure legend, the reader is referred to the web version of this article.)

Table 2
Mineralogical compositions of selected samples.

Sample no.	Bulk composition (ref.%)							Clay composition (ref.%)
	Qtz	Pl	Kfs	Dol	Gp	Anh	Clay	Ill
An-01 (||)	–	–	–	10.5	0.5	89	–	–
Dol-An-01 (||)	2.4	0.4	2.4	40	0.2	53.6	1	100
Dol-An-02 (⊥)	0.5	–	–	92.9	–	0.7	5.9	100

Qtz, quartz; Pl, plagioclase; Kfs, K-feldspar; Dol, Dolomite; Gp, gypsum; Anh, anhydrite; Clay, total clay; Ill, illite.

both the hydraulic conductivity and mechanical behavior of fault zones over seismic cycles (Evans and Chester, 1995; Haines and van der Pluijm, 2012; Heap et al., 2019). The presence of soluble feldspars in Dol-Anh-01, coupled with the progressive increase in illite content across damaged samples, strongly suggests fluid-mediated alteration processes (Fig. 5D-E; Table 2), consistent with documented fault-zone diagenesis (Solum et al., 2005; Haines and van der Pluijm, 2012; Duan et al., 2016). Given the well-developed deep-seated faults in this region (Jia et al., 2006; Hubbard et al., 2010; Lu et al., 2019), we infer that deep hydrothermal fluids may have contributed to feldspar formation. However, this hypothesis requires further investigation.

As established by previous studies (Rojstaczer and Wolf, 1992; Uehara and Shimamoto, 2004; Indrevaer et al., 2014), fault zones dynamically evolve between conduit and barrier states. Coseismic events typically generate transient permeability increases of one to three orders of magnitude through fracture creation and reactivation (Uehara and Shimamoto, 2004; Woodcock et al., 2007; De Paola et al., 2009; Manga et al., 2012; Frash et al., 2017). Post-seismic periods may further enhance permeability through dilation and brecciation, followed by long-term (10^2–10^3 yr) reduction due to compaction and mineralization (Fig. 6, Gratier, 2011). Our microstructural evidence—particularly anhydrite-filled fractures within dolostone—combined with low permeability values ($<10^{-18}$ m^2) suggest fracture healing and fault strength recovery during interseismic periods, forming an effective fluid barrier for both hydrocarbons and groundwater. Seismic reactivation, however, could temporarily transform damage zones into localized conduits through renewed fracturing (Figs. 5D-E, 6), indicating a time-dependent permeability behavior that fluctuates throughout the

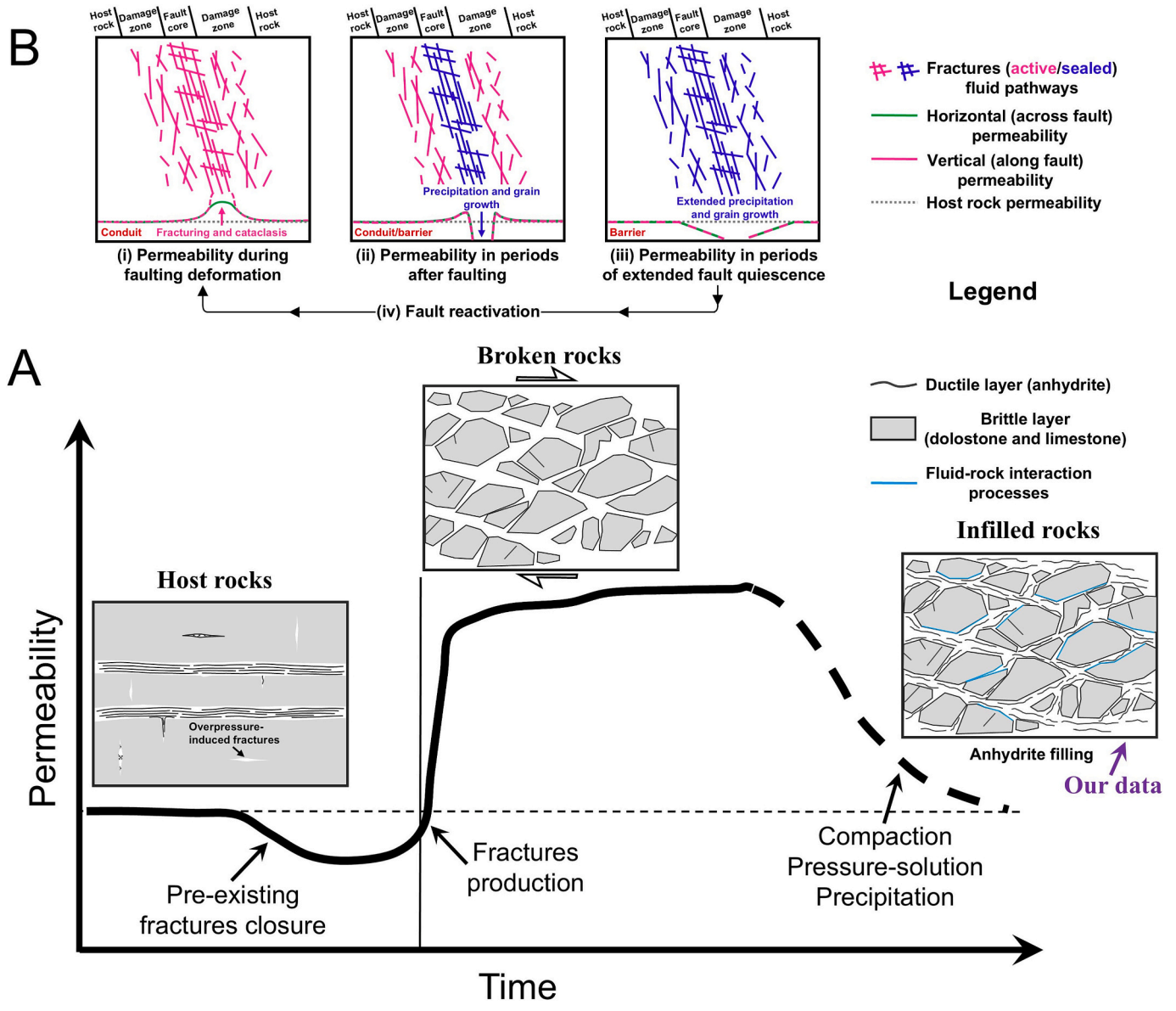

Fig. 6. (A) Schematic modal illustrating the permeability evolution of the evaporite-carbonate-hosted Triassic detachment fault zone throughout a seismic cycle (modified from Uehara and Shimamoto, 2004). (B) Conceptual model showing cyclic permeability evolution of a fault zone over geological time (Pei et al., 2015).

seismic cycle (Uehara and Shimamoto, 2004; Mitchell and Faulkner, 2008; Pei et al., 2015; Smeraglia et al., 2016; Yehya and Rice, 2020).

While this study provides important constraints on fault-zone hydraulic behavior, the assessment of coseismic fluid transport remains qualitative. We emphasize the need for quantitative investigations under varied thermal regimes, as temperature significantly impacts permeability (Faulkner, 2004; Kato et al., 2004). Future work should therefore prioritize triaxial permeability experiments on evaporite-carbonate cataclasite to better characterize coupled thermo-hydro-mechanical processes. Such studies will enhance our understanding of time-dependent fluid flow and mechanical recovery within seismically active fault zones.

5.2. *Pressure sensitivity coefficient (γ) analysis*

The corresponding pressure sensitivity coefficients (γ) range from 0.016 MPa^{-1} to 0.018 MPa^{-1} for the intact sample, and from 0.032 MPa^{-1} to 0.049 MPa^{-1} and 0.024 MPa^{-1} to 0.048 MPa^{-1} for the damaged samples Dol-Anh-01 and Dol-Anh-02, respectively. The mean γ values of the damaged samples are therefore approximately two to three times higher than those of the intact sample. Previous studies (Al-Wardy and Zimmerman, 2004; Ghabezloo and Sulem, 2009; Li et al., 2009) indicate that γ can reach values greater than 1 in clay-rich rocks due to the presence of soft phases or continuous pore structures. Vermylen (2011) also noted that such elevated values may arise from continuous flow paths within soft, porous kerogen. Considering the microstructural and mineralogical differences among our samples—specifically, the more developed structural features and higher abundance of weak-phase constituents in the damaged units (Fig. 5, Table 2)—the relative higher γ values in the damaged samples likely reflect the influence of soft constituents such as clay minerals and bitumen, together with the enhanced development of microporosity and microfractures (cf. Zoback and Harjes, 1997; Al-Wardy and Zimmerman, 2004; Ghabezloo and Sulem, 2009; Vermylen, 2011).

6. Conclusions

This study systematically characterizes the hydraulic properties of the Middle-Lower Triassic detachment fault zone through integrated mineralogical, permeability, and microstructural analyses of anhydrite-

dolostone cataclasite obtained from the LS1 borehole (~6900 m depth) in the frontal Longmen Shan. Our principal conclusions reveal:

(1) Fluid transport in these evaporite-carbonate units is dominantly regulated by brittle dolostone components, with secondary influences from weak-phase (i.e., clay) alignment and fluid-induced alteration processes.
(2) The fault zone exhibits dynamic permeability evolution, characterized by: i) Seismic-phase enhancement through fracture generation and reactivation; ii) Interseismic reduction via healing and compaction mechanisms; iii) Consistently low background permeability ($<10^{-18}$ m^2) at depth, establishing the fault as an effective fluid barrier during quiescent periods

These findings provide critical constraints for understanding fluid migration patterns and fault mechanics in evaporite-carbonate hosted detachment systems. The observed permeability variations have important implications for hydrocarbon migration and seismic hazard assessment in the Longmen Shan thrust belt, where fluid overpressures may influence fault slip behavior. Future studies should incorporate in situ stress measurements and long-term monitoring to better quantify the feedback between fluid flow and fault stability.

CRediT authorship contribution statement

Lin Zhang: Writing – original draft, Visualization, Validation, Software, Methodology, Formal analysis, Data curation, Conceptualization. **Yi Li:** Funding acquisition. **Qingbao Duan:** Data curation. **Shunjie Deng:** Data curation. **Nianfa Yang:** Data curation. **Huayao Zou:** Project administration. **Jianye Chen:** Project administration, Data curation. **Zonghu Liao:** Writing – review & editing, Supervision, Project administration, Funding acquisition.

Declaration of competing interest

The authors declare that they have no known competing financial interests or personal relationships that could have appeared to influence the work reported in this paper.

Acknowledgement

We thank Dr. Dancheng Zhu for technical support with optical microscopy. We acknowledge the China-Portugal Joint Laboratory on AI for Climate and Energy and the National Key Research and Development Program of China (2024YFE0114000).

Appendix A. Supplementary data

Supplementary data to this article can be found online at https://doi.org/10.1016/j.tecto.2025.230970.

Data availability

Data will be made available on request.

References

Agosta, F., Prasad, M., Aydin, A., 2007. Physical properties of carbonate fault rocks, Fucino basin (Central Italy): implications for fault seal in platform carbonates. Geofluids 7, 19–32.
Al-Wardy, W., Zimmerman, R.W., 2004. Effective stress law for the permeability of clay-rich sandstones. J. Geophys. Res. 109 (B4).
Antonellini, M., Aydin, A., 1994. Effect of faulting on fluid flow in porous sandstones: petrophysical properties. AAPG Bull. 78 (3), 355–377.
Bense, V., Gleeson, T., Loveless, S., Bour, O., Scibek, J., 2013. Fault zone hydrogeology. Earth Sci. Rev. 127, 171–192.
Berryman, J.G., 1992. Effective stress for transport properties of inhomogeneous porous rock. J. Geophys. Res. 97 (B12), 409–17424, 17.
Bos, B., Spiers, C.J., 2002. Fluid-assisted healing processes in gouge-bearing faults: insights from experiments on a rock analogue system. Pure Appl. Geophys. 159, 2537–2566.
Burchfiel, B.C., Chen, Z., Liu, Y., Royden, L.H., 1995. Tectonics of the Longmen Shan and adjacent regions. Int. Geol. Rev. 37, 661–738.
Caine, J.S., Evans, J.P., Forster, C.B., 1996. Fault zone architecture and permeability structure. Geology 24 (11), 1025–1028.
Chen, S., Wilson, C.G.L., 1996. Emplacement of the Longmen Shan thrust-nappe belt along the eastern margin of the Tibetan Plateau. J. Struct. Geol. 18 (4), 413–430.
Chen, S., Wilson, C.J.L., Worley, B.A., 1995. Tectonic transition from the Songpan-Garzè Fold Belt to the Sichuan Basin, South-Western China. Basin Res. 7 (3), 235–253.
Chen, J.Y., Yang, X.S., Duan, Q.B., Shimamoto, T., Spiers, C.J., 2013. Importance of thermochemical pressurization in the dynamic weakening of the Longmenshan Fault during the 2008 Wenchuan earthquake: Inferences from experiments and modeling. J. Geophys. Res. 118, 4145–4169.
Chen, J.Y., Yang, X.S., Duan, Q.B., Peach, C., 2015. Integrated measurements of permeability, effective porosity, and specific storage of core samples using water as the pore fluid. Int. J. Rock Mech. Min. Sci. 79, 55–62.
Chester, F.M., Evans, J.P., Biegel, R.L., 1993. Internal structure and weakening mechanisms of the San Andreas Fault. J. Geophys. Res. Solid Earth 98 (B1), 771–786.
Curzi, M., Aldega, L., Billi, A., Boschi, C., Carminati, E., Vignaroli, G., Viola, G., Bernasconi, S., 2024. Fossil chemical-physical (dis)equilibria between paleo fluids and host rocks and their relationship to the seismic cycle and earthquakes. Earth Sci. Rev. 254, 104801.
David, C., Wang, T., Zhu, W., Zhang, J., 1994. Laboratory measurement of compaction-induced permeability change in porous rocks: implications for the generation and maintenance of pore pressure excess in the crust. Pure Appl. Geophys. 143, 425–456.
David, C., Menendez, B., Zhu, W., Wang, T.-F., 2001. Mechanical compaction, microstructures and permeability evolution in sandstones. Phys. Chem. Earth Solid Earth Geod. 26 (1–2), 45–51.
De Paola, N., Collettini, C., Faulkner, D.R., Trippetta, F., 2008. Fault zone architecture and deformation processes within evaporitic rocks in the upper crust. Tectonics 27 (TC4017).
De Paola, N., Faulkner, D., Collettini, C., 2009. Brittle versus ductile deformation as the main control on the transport properties of low-porosity anhydrite rocks. J. Geophys. Res. 114.
Duan, Q.B., Yang, X.S., Ma, S.L., Chen, J.Y., Chen, J.Y., 2016. Fluid–rock interactions in seismic faults: Implications from the structures and mineralogical and geochemical compositions of drilling cores from the rupture of the 2008Wenchuan earthquake, China. Tectonophysics 666, 260–280.
Duan, Q.B., Yang, X.S., Chen, J.Y., 2017. Hydraulic properties of a low permeable rupture zone on the Yingxiu-Beichuan Fault activated during the Wenchuan earthquake, China: implications for fluid conduction, fault sealing, and dynamic weakening mechanisms. Tectonophysics 721, 123–142.
Dvory, N., Zoback, M., 2021. Prior oil and gas production can limit the occurrence of injection-induced seismicity: a case study in the Delaware Basin of western Texas and southeastern New Mexico, USA. Geology 49, 1198–1203.
Evans, J., Chester, F., 1995. Fluid-rock interaction in faults of the San Andreas system: Inferences from San Gabriel fault rock geometry and microstructures. J. Geophys. Res. 100, 13007–13020.
Evans, J., Forster, G., Goddard, J., 1997. Permeability of fault-related rocks for hydraulic structure of fault zones. J. Struct. Geol. 19, 1393–1404.
Faulkner, D.R., 2004. A model for the variation in permeability of clay-bearing fault gouge with depth in the brittle crust. Geophys. Res. Lett. 31 (L19611).
Faulkner, D., Jackson, C., Lunn, R., Schlische, R., Shipton, Z., Wibberley, C., Withjack, M., 2010. A review of recent developments connecting the structure, mechanics and fluid flow properties of fault zones. J. Struct. Geol. 32, 1557–1575.
Fischer, G.J., 1992. The determination of permeability and storage capacity: pore pressure oscillation method. In: Evans, B., Wang, T.-F. (Eds.), Fault Mechanics and Transport Properties of Rocks. Academic Press, London, pp. 187–211.
Fischer, G.J., Paterson, M.S., 1992. Measurement of permeability and storage capacity in rocks during deformation at high temperature and pressure. In: Evans, B., Wang, T.-F. (Eds.), Fault Mechanics and Transport Properties of Rocks. Academic Press, London, pp. 213–252.
Frash, L., Garey, J., Ickes, T., Viswanathan, H., 2017. Caprock integrity susceptibility to permeable fracture creation. Int. J. Greenh. Gas Control. 64, 60–72.
Ghabezloo, S., Sulem, J., 2009. Stress dependent thermal pressurization of a fluid-saturated rock. Rock Mech. Rock. Eng. 42, 1–24.
Gratier, J., 2011. Fault permeability and strength evolution related to fracturing and healing episodic processes (years to Millennia): the role of pressure solution. Oil Gas Sci. Technol. Rev. IFP Energies Nouv. 66, 491–506.
Guo, H., Brodsky, E.E., Geobel, T.H.W., Cladouhos, T.T., 2021. Measuring fault zone and host rock hydraulic properties using tidal responses. Geophys. Res. Lett. 48 (13).
Haines, S.H., van der Pluijm, B., 2012. Patterns of mineral transformations in clay gouge, with examples from low-angle normal fault rocks in the western USA. J. Struct. Geol. 43, 2–32.
Haines, T., Michie, E., Neilson, J., Healy, D., 2016. Permeability evolution across carbonate hosted normal fault zones. Mar. Pet. Geol. 72, 62–82.
Heap, M., Troll, V., Kushnir, A., Gilg, H., Collinson, A., Deegan, F., Darmawan, H., Seraphine, N., Neuberg, J., Walter, T., 2019. Hydrothermal alteration of andesitic lava domes can lead to explosive volcanic behaviour. Nat. Commun. 10.
Hubbard, J., Shaw, J.H., 2009. Uplift of the Longmen Shan and Tibetan Plateau, and the 2008 Wenchuan (M = 7.9) earthquake. Nature 458, 194–197.
Hubbard, C.R., Evans, E.H., Smith, D.K., 1976. The reference intensity ratio, I/Ic, for computer simulated powder patterns. J. Appl. Crystallogr. 9 (2), 169–174.

Hubbard, J., Shaw, J., Klinger, Y., 2010. Structural setting of the 2008 Mw 7.9 Wenchuan, China, earthquake. Bull. Seismol. Soc. Am. 100 (5B), 2713–2735.
Indrevaer, K., Stunitz, H., Bergh, S., 2014. On Palaeozoic-Mesozoic brittle normal faults along the SW Barents Sea margin: fault processes and implications for basement permeability and margin evolution. J. Geol. Soc. Lond. 171 (6), 831–846.
Jia, D., Wei, G., Chen, Z., Li, B., Zeng, Q., Yang, G., 2006. Longmen Shan fold-thrust belt and its relation to the western Sichuan Basin in Central China: new insights from hydrocarbon exploration. AAPG Bull. 90, 1425–1447.
Jia, D., Li, Y., Lin, A., Wang, M., Chen, W., Wu, X., Ren, Z., Zhao, Y., Luo, L., 2010. Structural model of 2008 Mw 7.9 Wenchuan earthquake in the rejuvenated Longmen Shan thrust belt, China. Tectonophysics 491, 174–184.
Kato, A., Sakaguchi, A., Yoshida, S., Yamaguchi, H., Kaneda, Y., 2004. Permeability structure around an ancient exhumed subduction-zone fault. Geophys. Res. Lett. 31 (6), L06602.
Kim, Y.S., Peacock, D.C.P., Sanderson, D.J., 2004. Fault damage zones. J. Struct. Geol. 26 (3), 503–517.
Kitagawa, Y., Koizumi, N., Notsu, K., Igarashi, G., 1999. Water injection experiments and discharge changes at the Nojima Fault in Awaji Island, Japan. Geophys. Res. Lett. 26 (20), 3173–3176.
Lacroix, B., Charpentier, D., Buatier, M., Vennemann, T., Labaume, P., Adatte, T., Trave, A., Dubois, M., 2012. Formation of chlorite during thrust fault reactivation. Record of fluid origin and P-T conditions in the Monte Perdido thrust fault (southern Pyrenees). Contrib. Mineral. Petrol. 163, 1083–1102.
Leclere, H., Faulkner, D., Wheeler, J., Mariani, E., 2016. Permeability control on transient slip weakening during gypsum dehydration: implications for earthquakes in subduction zones. Earth Planet. Sci. Lett. 442, 1–12.
Li, Y., Zeng, Y., Yi, H., 1995. Sedimentary and Tectonic Evolution of the Longmen Shan Foreland Basin, western Sichuan, China. Press of Chengdu University of Science and Technology, Chengdu, pp. 1–92 (in Chinese).
Li, M., Bernabe, Y., Xiao, W., Chen, Z., Liu, Z., 2009. Effective pressure law for permeability of E-bei sandstones. J. Geophys. Res. 114 (B07205).
Li, Z., Liu, S., Chen, H., Deng, B., Hou, M., Wu, W., Cao, J., 2012. Spatial variation in Meso-Cenozoic exhumation history of the Longmen Shan thrust belt (eastern Tibetan Plateau) and the adjacent western Sichuan basin: Constraints from fission track thermochronology. J. Asian Earth Sci. 47, 185–203.
Li, Z., Liu-Zeng, J., Jia, D., Sun, C., Wang, W., Yuan, Z., Liu, B., 2016. Quaternary activity of the range front thrust system in the Longmen Shan piedmont, China, revealed by seismic imaging and growth strata. Tectonics 35 (12), 2807–2827.
Li, Z., Zhang, P., Zheng, W., Jia, D., Hubbard, J., Almeida, R., Sun, C., Shi, X., Li, T., 2018. Oblique thrusting and strain partitioning in the Longmen Shan fold-and-thrust belt, eastern Tibetan Plateau. J. Geophys. Res. 123 (5), 4431–4453.
Liao, Z., Zhang, L., Zou, H., Hao, F., Reches, Z., 2023. Damage stratigraphy as a controlling mechanism of earthquakes distribution and fault patterns. Tectonophysics 846.
Liu, S., Luo, Z., Dai, S., Dennis, A., Wilson, C.J.L., 1996. The uplift of the Longmenshan thrust belt and subsidence of the West Sichuan Foreland Basin. Acta Geol. Sin. 9, 16–26 (in Chinese).
Liu, S., Li, Z., Cao, J., Liu, S., Deng, B., Wang, G., 2009. 4-D textural and structural characteristics of Longmen intracontinental composite orogenic belt, Southwest China. Chin. J. Geol. 44 (4), 1151–1180 (in Chinese).
Lockner, D., Naka, H., Tanaka, H., et al., 2000. Permeability and strength of core samples from the Nojima fault of the 1995 Kobe earthquake. In: Proceedings of the International Workshop on the Nojima Fault Core and Borehole Analysis. US Geological Survey, pp. 22–23.
Lu, R., He, D., Suppe, J., Ma, Y., Liu, B., Chen, Y., 2012. Along-strike variation of the frontal zone structural geometry of the Central Longmen Shan thrust belt revealed by seismic reflection profiles. Tectonophysics 580, 178–191.
Lu, R., He, D., Xu, X., Tan, X., Li, Y., Cai, M., Wang, Z., 2019. Geometry and kinematics of buried structures in the piedmont of the Central Longmen Shan: implication for the growth of the Eastern Tibetan Plateau. J. Geol. Soc. Lond. 176, 323–333.
Manga, M., Beresnev, I., Brodsky, E., Elkhoury, J., Elsworth, D., Ingebritsen, S., Mays, D., Wang, C., 2012. Changes in permeability caused by transient stresses: field observations, experiments, and mechanisms. Rev. Geophys. 50.
Mitchell, T., Faulkner, D., 2008. Experimental measurements of permeability evolution during triaxial compression of initially intact crystalline rocks and implications for fluid flow in fault zones. J. Geophys. Res. 113 (B11412).
Mizoguchi, K., Hirose, T., Shimamoto, T., Fukuyama, E., 2008. Internal structure and permeability of the Nojima fault, Southwest Japan. J. Struct. Geol. 30, 513–524.
Molli, G., Cortecci, G., Vaselli, L., Ottria, G., Cortopassi, A., Dinelli, E., Mussi, M., Barbieri, M., 2010. Fault zone structure and fluid–rock interaction of a high angle normal fault in Carrara marble (NW Tuscany, Italy). J. Struct. Geol. 32, 1334–1348.
Molnar, P., Tapponnier, P., 1975. Cenozoic tectonics of Asia: effects of continental collision. Science 189 (4201), 419–426.
Morrow, C.A., Zhang, B., Byerlee, J.D., 1986. Effective pressure law for permeability of Westerly Granite under cyclic loading. J. Geophys. Res. 91 (B3), 3870–3876.
Morrow, C.A., Lockner, D.A., Moore, D.E., Hickman, S., 2014. Deep permeability of the San Andreas fault from San Andreas fault observatory at depth (SAFOD) core samples. J. Struct. Geol. 64, 99–114.
Ohtake, M., 1974. Seismic activity induced by water injection at Matsushiro, Japan. J. Phys. Earth. 22, 163–176.
Pei, Y., Paton, D., Knipe, R., Wu, K., 2015. A review of fault sealing behaviour and its evaluation in siliciclastic rocks. Earth Sci. Rev. 150, 121–138.
Rempe, M., Mitchell, T., Renner, J., Smith, S., Bistacchi, A., Di Toro, G., 2018. The relationship between microfracture damage and the physical properties of fault-related rocks: the Gole Larghe fault zone, Italian southern Alps. J. Geophys. Res. Solid Earth 123 (9), 7661–7687.
Rojstaczer, S., Wolf, S., 1992. Permeability changes associated with large earthquakes: an example from Loma Prieta, California. Geology 20, 211–214.
Ross, Z.E., Cochran, E.S., Trugman, D.T., Smith, J.D., 2020. 3D fault architecture controls the dynamism of earthquake swarms. Science 368 (6497), 1357–1361.
Sagy, A., Reches, Z., Roman, I., 2001. Dynamic fracturing: field and experimental observations. J. Struct. Geol. 23 (8), 1223–1239.
Savage, H., Brodsky, E., 2011. Collateral damage: evolution with displacement of fracture distribution and secondary fault strands in fault damage zones. J. Geophys. Res. Solid Earth 116 (B03405).
Schon, J., 1996. Physical properties of rocks: fundamentals and principles of petrophysics. In: Handbook of Geophysical Exploration 8. Pergamon Press, London.
Scibek, J., 2020. Multidisciplinary database of permeability of fault zones and surrounding protolith rocks at world-wide sites. Sci Data 7, 95.
Smeraglia, L., Trippetta, F., Carminati, E., Mollo, S., 2014. Tectonic control on the petrophysical properties of foredeep sandstone in the Central Apennines, Italy. J. Geophys. Res. Solid Earth 119 (12), 9077–9094.
Smeraglia, L., Berra, F., Billi, A., Boschi, C., Carminati, E., Doglioni, C., 2016. Origin and role of fluids involved in the seismic cycle of extensional faults in carbonate rocks. Earth Planet. Sci. Lett. 450, 292–305.
Smeraglia, L., Aldega, L., Bernasconi, S., et al., 2020. The Role of trapped fluids during the development and deformation of a carbonate/shale intra-wedge tectonic melange (Mt. Massico, Southern Apennines, Italy). J. Struct. Geol. 138.
Smeraglia, L., Fabbi, S., Billi, A., Carminati, E., Cavinato, G., 2022. How hydrocarbons move along faults: evidence from microstructural observations of hydrocarbon-bearing carbonate fault rocks. Earth Planet. Sci. Lett. 584, 117454.
Solum, J.G., van der Pluijm, B.A., Peacor, D.R., 2005. Neocrystallization, fabrics and age of clay minerals from an exposure of the Moab Fault, Utah. J. Struct. Geol. 27, 1563–1576.
Sutherland, R., Toy, V.G., Townend, J., Cox, S.C., Eccles, J.D., Faulkner, D.J., Kopf, A.J., 2012. Drilling reveals fluid control on architecture and rupture of the Alpine fault, New Zealand. Geology 40, 1143–1146.
Tanikawa, W., Shimamoto, T., 2009. Comparison of Klinkenberg-corrected gas permeability and water permeability in sedimentary rocks. Int. J. Rock Mech. Min. Sci. 46, 229–238.
Tanikawa, W., Hirose, T., Mukoyoshi, H., Tadai, O., Lin, W., 2013. Fluid transport properties in sediments and their role in large slip near the surface of the plate boundary fault in the Japan Trench. Earth Planet. Sci. Lett. 382, 150–160.
Townend, J., Zoback, M.D., 2000. How faulting keeps the crust strong. Geology 28 (5), 399–402.
Trippetta, F., Collettini, C., Vinciguerra, S., Meredith, P.G., 2010. Laboratory measurements of the physical properties of Triassic Evaporites from Central Italy and correlation with geophysical data. Tectonophysics 492, 121–132.
Tsutsumi, A., Nishino, S., Mizoguchi, K., Hirose, T., Uehara, S., Sato, K., Tanikawa, W., Shimamoto, T., 2004. Principal fault zone width and permeability of the active Neodani fault, Nobi active fault system, Southwest Japan. Tectonophysics 379, 93–108.
Uehara, S., Shimamoto, T., 2004. Gas permeability evolution of cataclasite and fault gouge in triaxial compression and implications for changes in fault-zone permeability structure through the earthquake cycle. Tectonophysics 378, 183–195.
Uehara, S., Shimamoto, T., Okazaki, K., Funaki, H., Kurikami, H., Niizato, T., Ohnishi, Y., 2012. Can surface samples be used to infer underground permeability structure? A test case for Neogene sedimentary basin in horonobe, Japan. Int. J. Rock Mech. Min. Sci. 56, 1–14.
Vermylen, J.P., 2011. Geomechanical Studies of the Barnett Shale, 143. Stanford University, Texas, USA (PhD thesis).
Wang, M., Jia, D., Shaw, J., Hubbard, J., Plesch, A., Li, Y., Liu, B., 2014. The 2013 Lushan earthquake: implications for seismic hazards posed by the Range Front blind thrust in the Sichuan Basin, China. Geology 42, 915–918.
Wang, H., Xu, W., Cai, M., Xiang, Z., Kong, Q., 2017. Gas permeability and porosity evolution of a porous sandstone under repeated loading and unloading conditions. Rock Mech. Rock. Eng. 50, 2071–2083.
Wibberley, C.A.J., Shimamoto, T., 2003. Internal structure and permeability of major strike-slip fault zones: the median Tectonic Line in Mie Prefecture, Southwest Japan. J. Struct. Geol. 25, 59–78.
Wilson, C.R., Doe, T.W., Long, J.C.S., Witherspoon, P.A., 1979. Permeability characterization of nearly impermeable rock masses for nuclear waste repository siting. In: Proceedings of the OECD Symposium on Well Testing in Low Permeability Rocks, Paris.
Woodcock, N.H., Dickson, J.A.D., Tarasewicz, J.P.T., 2007. Transient permeability and reseal hardening in fault zones: evidence from dilation breccia textures.
Xue, L., Li, H.B., Brodsky, E.E., Xu, Z.Q., Kano, Y., Wang, H., Mori, J.J., Si, J.L., Pei, J.L., Zhang, W., Yang, G., Sun, Z.M., Huang, Y., 2013. Continuous permeability measurements record healing inside the Wenchuan earthquake fault zone. Science 340 (6140), 1555–1559.
Yan, R., Wang, G.C., Shi, Z.M., 2016. Sensitivity of hydraulic properties to dynamic strain within a fault damage zone. J. Hydrol. 543, 721–728.
Yehya, A., Rice, J.R., 2020. Influence of fluid-assisted healing on fault permeability structure. J. Geophys. Res. Solid Earth 125 (10).
Zhang, L., Liao, Z., Long, K., Carpenter, B.M., Zou, H., Hao, F., 2022. Fundamental constraints of lithologically-controlled fault networks on gas migration and accumulation for fractured carbonates in the western Sichuan Basin, China. J. Pet. Sci. Eng. 208.
Zoback, M.D., Harjes, H.P., 1997. Injection-induced earthquakes and crustal stress at 9 km depth at the KTB deep drilling site, Germany. J. Geophys. Res. 102 (B8), 18477–18491.